Chinese Chemical Letters 36 (2025) 110003

Contents lists available at ScienceDirect

Chinese Chemical Letters

journal homepage: www.elsevier.com/locate/cclet

Photosensitizer-synergized g-carbon nitride nanosheets with enhanced photocatalytic activity for eradicating drug-resistant bacteria and promoting wound healing

Yueying Wang[a,1], Jianming Xiong[b,1], Linwei Xin[a], Yuanyuan Li[c,*], He Huang[d,*], Wenjun Miao[b,e,*]

[a] College of Biotechnology and Pharmaceutical Engineering, Nanjing Tech University, Nanjing 211816, China
[b] School of Pharmaceutical Sciences, Nanjing Tech University, Nanjing 211816, China
[c] School of Pharmacy, Hainan Medical University, Haikou 571199, China
[d] School of Food Science and Pharmaceutical Engineering, Nanjing Normal University, Nanjing 210023, China
[e] State Key Laboratory of Materials-Oriented Chemical Engineering, Nanjing Tech University, Nanjing 211816, China

ARTICLE INFO

Article history:
Received 14 March 2024
Revised 6 May 2024
Accepted 11 May 2024
Available online 12 May 2024

Keywords:
Graphitic carbon nitride
Photosensitizer
Photocatalytic
Antibacterial
Photodynamic therapy

ABSTRACT

The rapid emergence of drug-resistant bacterial strains undermines the efficacy of conventional antibiotics, necessitating the development of alternative therapies. Antimicrobial photodynamic therapy (PDT) is a promising approach, but its effectiveness is often limited by the suboptimal photocatalytic activity of photosensitizers. In this study, we introduce a novel photoresponsive carbon-based antibacterial agent, Ce6/g-C_3N_4, which combines the photocatalytic properties of graphite-phase carbon nitride (g-C_3N_4) with the photodynamic attributes of chlorin e6 (Ce6). This agent, with an average particle size of 250.7 nm, demonstrates significantly enhanced photocatalytic activity. Additionally, the strong affinity of Ce6/g-C_3N_4 for bacteria and efficient delivery of Ce6 result in an inhibition rate exceeding 99% against Gram-positive bacteria and excellent biofilm eradication under light irradiation. *In vivo* experiments reveal that Ce6/g-C_3N_4 effectively inhibits bacterial growth on wounds, and promotes wound healing post-light treatment, while maintaining good biocompatibility. Overall, the Ce6/g-C_3N_4 antibacterial agent synergizes photodynamic and photocatalytic mechanisms, offering a new avenue for the photo-mediated, multi-strategic treatment of bacterial infections and wound healing.

The growing prevalence of drug-resistant bacteria poses a significant threat to global health, with recent data indicating an alarming increase in the emergence and spread of resistant strains. This trend undermines the effectiveness of existing antibiotics and necessitates the development of innovative treatments. Antibacterial photodynamic therapy (PDT) stands out as a viable alternative [1,2], using light-activated photosensitizers to generate reactive oxygen species (ROS) that effectively kill bacteria without fostering resistance [3-5]. However, the efficacy of current PDT methods is limited by the insufficient photocatalytic activity of photosensitizers, particularly against dense populations of drug-resistant bacteria [6]. Therefore, developing photosensitizers with enhanced photocatalytic activity is crucial for more effective infection treatments.

Graphitic carbon nitride (g-C_3N_4) nanosheets have been recognized for their unique properties, including stability, eco-friendliness, good biocompatibility and inherent photocatalytic activity under light irradiation [7-10], which is highly favorable for achieving antibacterial PDT purposes and rarely seen in other candidates such as polymeric and metal-based materials. Strategies such as heterostructuring [11-13], doping [14-16], and morphology control [17,18] have significantly improved their photocatalytic activity. In addition, the nanoscale form of g-C_3N_4 benefits from reduced diffusion distances and a larger specific surface area, leading to improved photocatalytic activity compared to traditional bulk materials [19]. Dye-sensitization of g-C_3N_4 nanosheets, in particular, effectively harnesses visible light and ensures safety [20-23], marking a promising research area. Lu's group demonstrate that when mesoporous g-C_3N_4 is sensitized with Eosin Y, its light absorption capacity is significantly enhanced, extending to longer

* Corresponding authors.
E-mail addresses: liyuanyuan@hainmc.edu.cn (Y. Li), huangh@njnu.edu.cn (H. Huang), miaowj@njtech.edu.cn (W. Miao).
[1] These authors contributed equally to this work.

https://doi.org/10.1016/j.cclet.2024.110003
1001-8417/

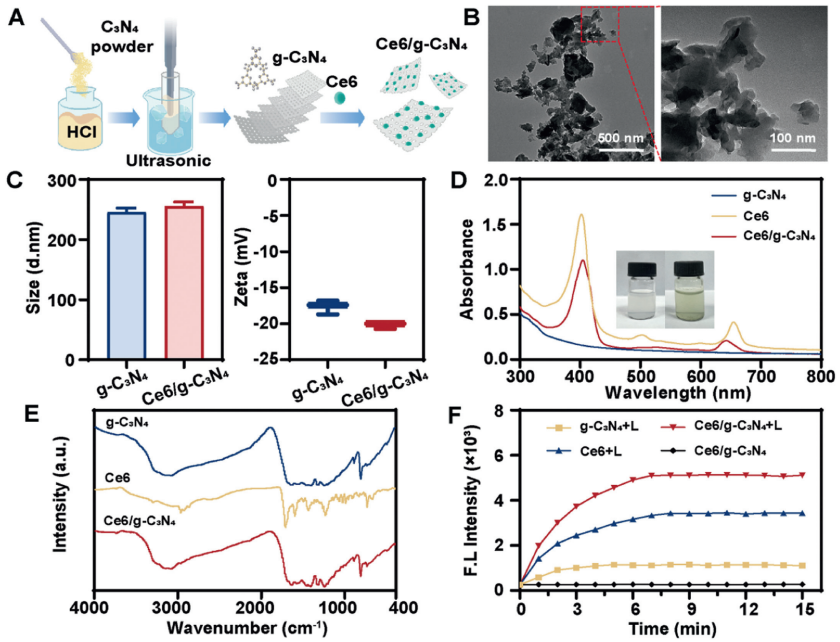

Fig. 1. Characterization of Ce6/g-C_3N_4. (A) Schematic diagram of construction of Ce6/g-C_3N_4 antibacterial agent. (B) TEM images of g-C_3N_4. Scale bar: 500 nm (left) and 100 nm (right). (C) Hydrodynamic particle size and zeta potential. Data are presented as mean ± standard deviation (s.d.) ($n = 3$). (D) Ultraviolet–visible (UV–vis) spectrum. Inset: pictures of g-C_3N_4 (left) and Ce6/g-C_3N_4 (right) aqueous suspension. (E) FT-IR spectrum. (F) Singlet oxygen generation of free Ce6, g-C_3N_4 and Ce6/g-C_3N_4 when irradiated with light (100 mW/cm^2) determined by SOSG.

wavelengths, which leads to increased hydrogen evolution activity under visible light irradiation [24]. However, the use of dye-sensitized g-C_3N_4 nanosheets in PDT for infection treatment and wound healing remains largely unexplored, presenting an opportunity for groundbreaking medical research advancements.

In this study, we combined photocatalytic acid-etched g-C_3N_4 with chlorin e6 (Ce6) to construct a novel nanosized photosensitizer, Ce6/g-C_3N_4, with enhanced photodynamic activity for eradicating drug-resistant bacteria and promoting wound healing. The fabrication process involves acid etching and stripping of bulk g-C_3N_4 [25], followed by the physical adsorption of Ce6 (Fig. 1A). The resulting g-C_3N_4 nanosheets exhibited typical 2-D lamellar structure with curling and stacking (Fig. 1B), as revealed by transmission electron microscope images. The particle size of g-C_3N_4 nanosheets was measured at 238.7 ± 2.83 nm, which was comparable to that of the Ce6/g-C_3N_4 nanosheets at 250.7 ± 6.61 nm (Fig. 1C), indicating the successful adsorption of negatively charged Ce6. The drug loading rate and encapsulation efficiency was determined to be 12.0% ± 3.9% and 94.3% ± 2.9%, respectively.

Spectral analysis (Fig. 1D) revealed that while g-C_3N_4 showed no absorption peaks in the 300–800 nm range, Ce6/g-C_3N_4 exhibited two distinct peaks at 405 and 642 nm, corresponding to the characteristic Soret-band and Q-band of [26], indicating successful integration of Ce6 with g-C_3N_4. X-ray diffraction (XRD) analysis (Fig. S1 in Supporting information) demonstrated that both bulk C_3N_4 and g-C_3N_4 nanosheets exhibited characteristic peaks at 13.0° and 27.6°, representing the (100) and (002) diffraction planes, respectively. The reduced intensity of the 27.6° peak after acid etching and mechanical stripping suggested increased disorder without altering the crystal structure [27]. Fourier-transform infrared (FT-IR) spectroscopy (Fig. 1E) showed absorption bands from 1200 cm^{-1} to 1700 cm^{-1} corresponded to C–N heterocycle stretching, while the peak at 807 cm^{-1} was associated with tri-*s*-triazine units [28,29]. Ce6/g-C_3N_4 retained the structural features of g-C_3N_4 and exhibited characteristic bands of Ce6, confirming the successful combination of g-C_3N_4 and Ce6. The photocatalytic activity of Ce6/g-C_3N_4, particularly its ability to generate singlet oxygen ($^1O_2$), was evaluated using SOSG kit. The fluorescence intensity of Ce6/g-C_3N_4 was notably higher than that of Ce6 after 15 min of light irradiation, indicating enhanced $^1O_2$ generation by the Ce6/g-C_3N_4 composite (Fig. 1F). Compared to other ways to achieve enhanced photocatalytic activity of g-C_3N_4, like element doping, structural modifications and quantum dot deposition, the photosensitizer-sensitization strategy employed here can expand the light absorption range, improve photon collection efficiency, provide additional excited electron pairs from the dye and accelerate charge transfer, thus realizing high efficiency photoelectric conversion. In addition, as shown in the electro paramagnetic resonance (EPR) spectra (Fig. S2 in Supporting information), $^1O_2$ was the primary reactive oxygen species (ROS) generated with Ce6/g-C_3N_4 under illumination. This finding is consistent with Ce6 mainly undergoing a type II photodynamic pathway, resulting in a high quantum yield of $^1O_2$. Only a minor amount of $O_2^{\bullet-}$ was induced as secondary ROS [30]. Collectively, Ce6/g-C_3N_4 efficiently produces $^1O_2$ under light irradiation, achieving synergistic antibacterial efficacy.

Flow cytometry was employed to study the bacterial association of Ce6/g-C_3N_4. Fig. 2A shows that Ce6/g-C_3N_4 nanosheets were effectively captured by methicillin-resistant *Staphylococcus aureus* (MRSA), and its fluorescence intensity was 1.7 times greater than Ce6 (Fig. 2B). This observation was likely due to the nanosheets structure and size effect Ce6/g-C_3N_4, resulting in a large specific surface area and more active sites for microbial interaction [31,32]. Scanning electron microscopy (SEM) images further confirmed this interaction, showing flake adhesion on the bacterial surface after treatment with Ce6/g-C_3N_4 (Fig. 2C). These results demonstrate that Ce6/g-C_3N_4 can efficiently deliver Ce6 to bacteria, offering significant advantages for effective antibacterial PDT. Figs. 2D–G display the bacterial colony growth and corresponding survival rate quantification after treatment with varying concentrations of Ce6, g-C_3N_4, and Ce6/g-C_3N_4. The results indicated that MRSA exhibited good survival in the absence of light across all groups, with no significant differences in colony numbers. However, under visible light, the number of colonies in the Ce6/g-C_3N_4-treated group was significantly reduced, demonstrating a concentration-

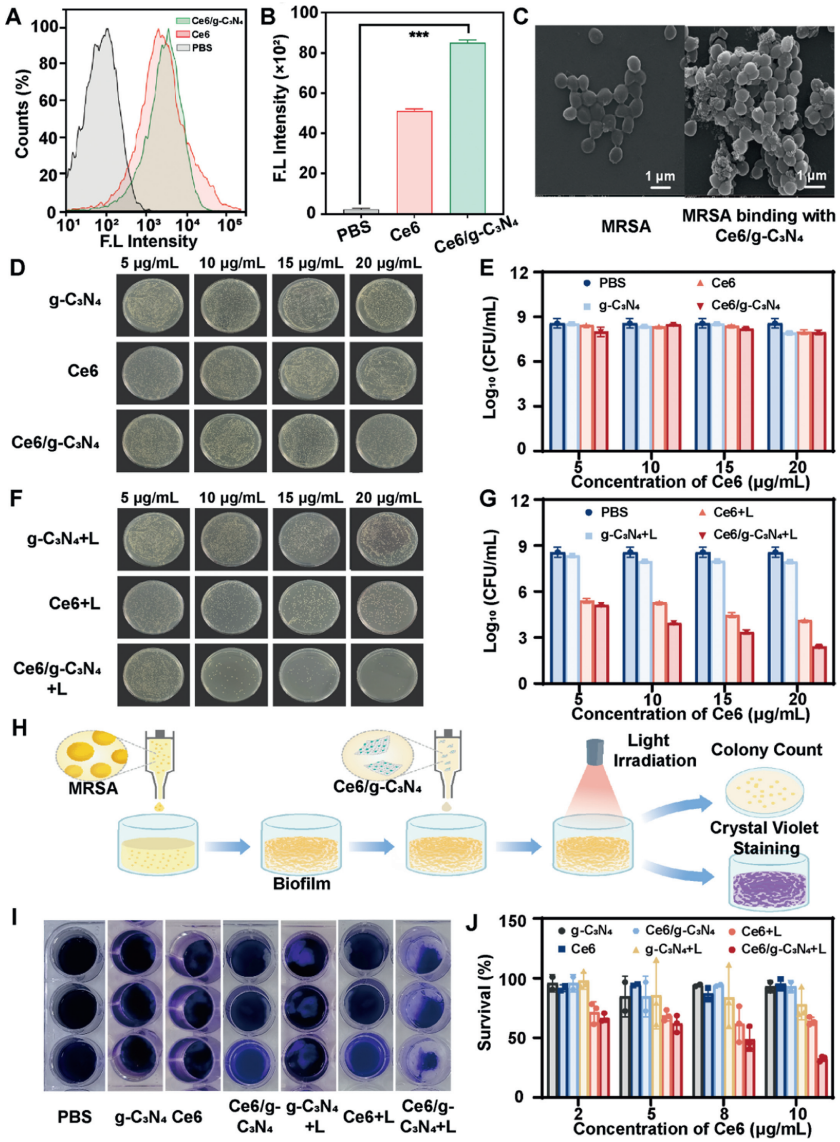

Fig. 2. Antibacterial activity *in vitro*. (A) Flow cytometric results and (B) quantitative fluorescence intensity of MRSA receiving treatment of Ce6/g-C_3N_4 and free Ce6. (C) SEM images of MRSA post-treatment. (D, F) Photographs of representative plate samples and (E, G) the corresponding colony forming units (CFU) number of MRSA treated with Ce6 or Ce6/g-C_3N_4 in dark (F, G) or with light (0.1 W/cm^2, 15 min). (H) Schematic diagram showing the antibiofilm test of Ce6/g-C_3N_4. (I) Crystal violet-stained MRSA biofilm following indicated treatment for 2 h and subsequent light irradiation (0.1 W/cm^2, 30 min). (J) Percentage of viable MRSA within biofilms. Data are presented as mean ± s.d. ($n = 6$). Scale bar: 1 μm. $^{***}P < 0.0001$.

dependent antibacterial effect. At 5 μg/mL, the bacterial survival rate decreased by 2 orders of magnitude (99% bactericidal rate), and at 20 μg/mL, MRSA was virtually eliminated, showcasing superior antimicrobial performance compared to Ce6 alone. These findings suggest that the combination of g-C_3N_4 and Ce6 provides enhanced photo-induced antibacterial activity, laying a solid foundation for rapid wound disinfection.

Biofilms contribute significantly to the ineffectiveness of antibiotics in chronic wound infections. It is essential to determine whether antibacterial agents can effectively ablate biofilms. A modified crystal violet staining method was employed to assess antibacterial biofilm formation, as depicted in Fig. 2H. Upon exposure to light, biofilms subjected to treatment with free Ce6 and g-C_3N_4 exhibited a dark purple coloration, while those treated with Ce6/g-C_3N_4 were visibly lighter (Fig. 2I). Both g-C_3N_4 and Ce6/g-C_3N_4-treated biofilms exhibited damage, possibly due to the lamellar structure of g-C_3N_4 disrupting bacterial metabolism and down-regulating biofilm-related genes [33]. Quantitative analysis (Fig. 2J) showed that the biomass of biofilms exposed to Ce6/g-C_3N_4 and light irradiation was reduced by 50% compared to those treated with free Ce6 at concentrations of 8 and 10 μg/mL. This indicates that Ce6/g-C_3N_4 has an excellent biofilm removal effect on antibiotic-resistant Gram-positive bacteria under visible light irradiation.

We further explored the wound healing effects of Ce6/g-C_3N_4-mediated PDT *in vivo* using a mouse epidermal MRSA-infected wound model. All animal studies were consistent with the guiding rules of the Animal Care Committee of Nanjing Tech University with approval (No. 20200914-01). The experimental setup is depicted in Fig. 3A, and the mice's vitality, weight changes, and wound healing were monitored daily. By day 4, all groups exhibited noticeable wound shrinkage and thin blood callus formation at the lesion edges (Fig. 3B). The Ce6/g-C_3N_4 with light irradiation group (Ce6/g-C_3N_4 + L) showed a significant improvement in wound closure rate compared to the PBS and non-irradiated groups, which displayed pus secretion around the wound on day 8 (Fig. 3C). The wound healing rate in Ce6/g-C_3N_4 + L group exceeded 90% by day 14, approximately 11% higher than the control.

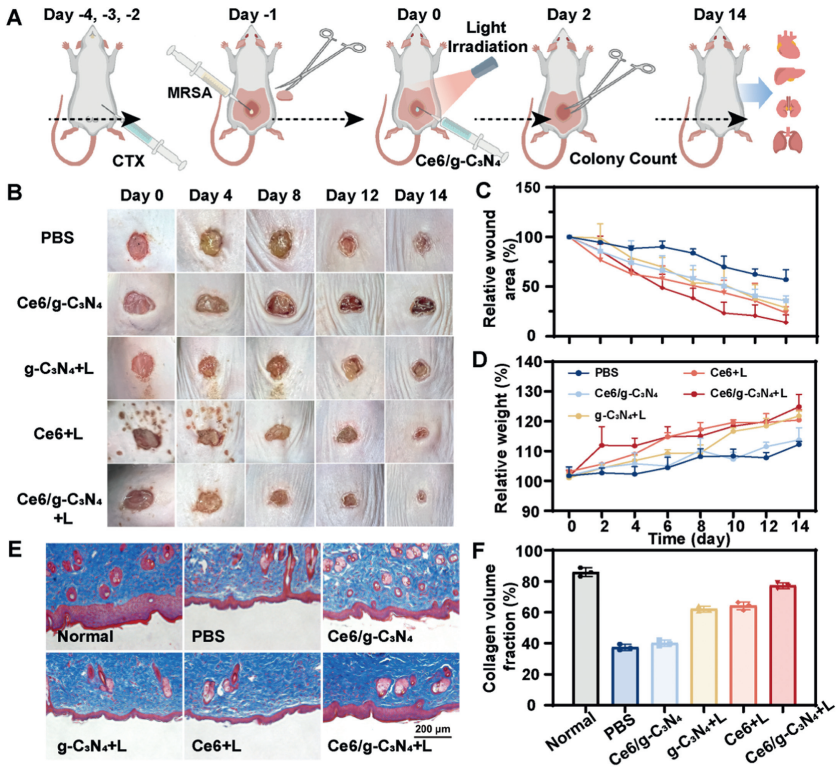

Fig. 3. Healing effects of Ce6/g-C_3N_4 on wounds infected with MRSA. (A) Scheme for *in vivo* study. (B) Photographs of MRSA-infected wounds of mice receiving indicated treatment. The dose of was 0.4 mg/kg. L denotes light irradiation at 0.1 W/cm^2 for 15 min. (C) Quantitative analysis of the wound area and (D) body weight change of mice infected with MRSA. (E) Masson's Trichrome staining of skin tissues of MRSA-infected mice on day 14. Scale bar: 200 μm. (F) Percentage of collagen volume fraction. Data are presented as mean ± s.d. ($n = 6$).

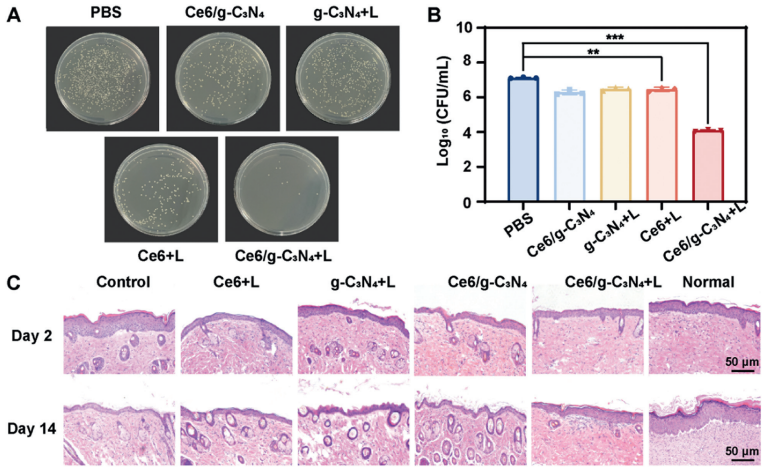

Fig. 4. Photodynamic antibacterial effectiveness of Ce6/g-C_3N_4 *in vivo* against MRSA-infected mice. (A) Representative images of MRSA colonies obtained from the infected sites of mice receiving indicated treatment on day 2. (B) Corresponding CFU count of MRSA from (A). (C) H&E-stained tissues from MRSA-infected mice on days 2 and 14 post treatments. L denotes light irradiation at 0.1 W/cm^2 for 15 min. Data are presented as mean ± s.d. ($n = 6$). $^{**}P < 0.001$, $^{***}P < 0.0001$. Scale bar: 50 μm.

In contrast, the PBS and dark treatment groups had larger unhealed wound areas with a volcanic appearance. Mice treated with Ce6/g-C_3N_4 + L showed a normal increase in body weight (Fig. 3D). Histological analysis on day 14 using Masson's trichrome staining revealed increased collagen production, with the proportion of collagen in the Ce6/g-C_3N_4 + L group reaching approximately 77.28%, compared to around 37.34% in the control group (Figs. 3E and F). This suggests that Ce6/g-C_3N_4 combined with light irradiation can accelerate the healing and tissue regeneration by promoting collagen production and deposition.

To further evaluate the therapeutic effect of Ce6/g-C_3N_4 on bacterial infections at wound sites, tissue samples were collected to assess bacterial presence in the skin after 2 days of treatment. As illustrated in Figs. 4A and B, there was a significant reduction in bacterial count in all treated groups compared to the control, with the most notable decrease observed in the Ce6/g-C_3N_4 + L group, confirming the strong photodynamic bactericidal efficacy of Ce6/g-C_3N_4. Moreover, hematoxylin and eosin (H&E) staining revealed intact epidermis in wound tissues treated with Ce6/g-C_3N_4 + L (Fig. 4C), suggesting successful wound healing and complete re-epithelialization and dermal regeneration.

To assess the cytocompatibility of Ce6/g-C_3N_4 *in vitro*, mouse skin fibroblasts (L929) were co-incubated with varying concentrations of g-C_3N_4 and Ce6/g-C_3N_4. Cell viability remained above 90%

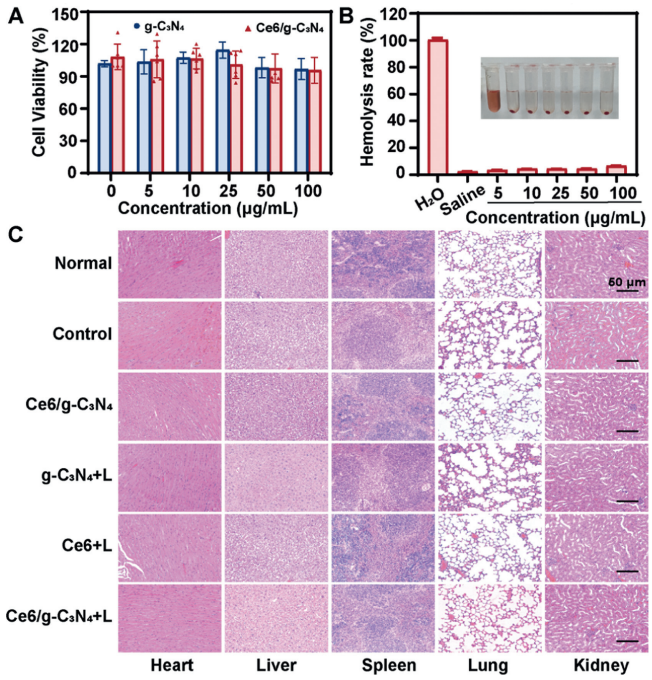

Fig. 5. Preliminary toxicity study. (A) Viabilities of L929 cells with treatment of g-C_3N_4 and Ce6/g-C_3N_4 for 24 h. (B) Hemolysis rates of Ce6/g-C_3N_4. Saline and H_2O were used as negative control and positive control, respectively. (C) H&E staining of major organs of MRSA-infected mice on day 14. Scale bar: 50 μm. L denotes light irradiation at 0.1 W/cm^2 for 15 min. Data are presented as mean ± s.d. ($n \geq 4$).

even at concentrations up to 100 μg/mL (equivalent to Ce6), suggesting minimal toxicity (Fig. 5A). Additionally, a hemolysis test confirmed the blood compatibility of Ce6/g-C_3N_4, with a negligible hemolysis rate (<10%) even at the highest concentration tested (Fig. 5B). To further evaluate *in vivo* safety, the major organs of mice were examined histologically. H&E staining revealed no significant abnormalities or damage in the treated groups compared to control mice (Fig. 5C). These findings suggest that Ce6/g-C_3N_4 possesses good biocompatibility and meets the basic requirements for biological materials, supporting its potential for safe application in antimicrobial PDT.

In conclusion, we developed a novel nanosized photosensitizer, Ce6/g-C_3N_4, by utilizing dye-sensitized g-C_3N_4, which exhibits enhanced photodynamic activity for eradicating resistant bacteria and promoting wound healing. The acid-etched g-C_3N_4 efficiently loads Ce6, allowing Ce6/g-C_3N_4 to retain the photodynamic activity of Ce6 while also improving singlet oxygen generation. Moreover, the effective delivery of Ce6 by Ce6/g-C_3N_4 enable rapid killing planktonic antibiotic-resistant bacteria and combating its biofilm under visible light irradiation. *In vivo* studies on epidermal MRSA-infected mice demonstrated successful wound healing, complete re-epithelialization, and dermal regeneration following treatment with Ce6/g-C_3N_4 and light irradiation. Preliminary toxicity studies also confirmed its negligible toxicity. Thus, Ce6/g-C_3N_4 emerges as a potent synergistic photosensitizer with enhanced photocatalytic activity for eradicating drug-resistant bacteria and accelerating wound healing, paving the way for the development of effective synergistic antimicrobial agents.

Declaration of competing interest

The authors declare that they have no known competing financial interests or personal relationships that could have appeared to influence the work reported in this paper.

CRediT authorship contribution statement

Yueying Wang: Writing – original draft, Investigation, Formal analysis. **Jianming Xiong:** Validation, Software, Investigation. **Linwei Xin:** Methodology. **Yuanyuan Li:** Writing – original draft, Funding acquisition. **He Huang:** Writing – review & editing, Supervision, Conceptualization. **Wenjun Miao:** Writing – review & editing, Supervision, Conceptualization.

Acknowledgments

This work was supported by the Natural Science Foundation of the Jiangsu Higher Education Institutes of China (No. 22KJB530006) and Hainan Provincial Natural Science Foundation of China (No. 824QN267).

Supplementary materials

Supplementary material associated with this article can be found, in the online version, at doi:10.1016/j.cclet.2024.110003.

References

[1] J. Zeng, Z. Li, H. Jiang, X. Wang, Mater. Horiz. 8 (2021) 2964–3008.
[2] M. Klausen, M. Ucuncu, M. Bradley, Molecules 25 (2020) 5239.
[3] T. Dougherty, C. Gomer, B. Henderson, et al., J. Natl. Cancer I. 90 (1998) 889–905.
[4] D. Dolmans, D. Fukumura, R. Jain, Nat. Rev. Cancer 3 (2003) 380–387.
[5] M. Broekgaarden, R. Weijer, T.M. Gulik, et al., Cancer Metast Rev. 34 (2015) 643–690.
[6] Y. Liu, X. Meng, W. Bu, Coordin. Chem. Rev. 379 (2019) 82–98.
[7] R. Huang, J. Wu, M. Zhang, et al., Mater. Des. 210 (2021) 110040.
[8] Y. Zhang, A. Thomas, M. Antonietti, X. Wang, J. Am. Chem. Soc. 131 (2009) 50–51.
[9] S. Yang, Y. Gong, J. Zhang, et al., Adv. Mater. 25 (2013) 2452–2456.
[10] U.S. Malik, Q. Duan, M.B.K. Niazi, et al., Chin. Chem. Lett. 34 (2023) 108071.
[11] Y. Li, S. Zhu, Y. Liang, et al., Mater. Des. 196 (2020) 109191.
[12] X. Guo, J. Duan, W. Wang, et al., Fuel 280 (2020) 118543.
[13] Y. Xing, X. Wang, S. Hao, et al., Chin. Chem. Lett. 32 (2021) 13–20.
[14] C. Liu, W. Wang, W. Hu, et al., J. Phys. Chem. Solid. 180 (2023) 111728.
[15] X. Hou, L. Cui, H. Du, et al., Appl. Catal. B: Environ. 278 (2020) 119253.
[16] L. Zhang, J. Liao, Y. Li, W. Sun, C. Ge, Chin. Chem. Lett. 35 (2024) 108568.
[17] Z. Fan, Y. Liu, X. Guo, Z. Jin, Int. J. Hydrog. Energ. 48 (2023) 19137–19152.
[18] Y. Gu, H. Feng, J. Zhao, et al., Chem. Eng. J. 476 (2023) 141645.
[19] Z. Tong, D. Yang, Z. Li, et al., ACS Nano 11 (2017) 1103–1112.
[20] S. Kang, L. Chen, S. Song, L. Yu, P. Zhang, Appl. Surface Sci. 258 (2012) 6029–6033.
[21] J. Xu, Y. Li, S. Peng, Int. J. Hydrog. Energy 40 (2015) 353–362.
[22] H. Dang, G. Tan, W. Yang, et al., J. Taiwan Inst. Chem. E 78 (2017) 185–194.
[23] S. Cao, J. Yu, Phys. Chem. Lett. 5 (2014) 2101–2107.
[24] S. Min, G. Lu, Phys. Chem. C 116 (2012) 19644–19652.
[25] S. Wu, C. Chen, W. Zhang, Chin. Chem. Lett. 25 (2014) 1247–1251.
[26] P. Li, G. Zhou, X. Zhu, et al., Photodiagn. Photodyn. 9 (2012) 76–82.
[27] Z. He, Z. Mo, J. Fu, et al., J. Alloy. Compd. 904 (2022) 163788.
[28] K. Zhang, L. Wang, X. Sheng, et al., Adv. Energy. Mater. 6 (2016) 1502352.
[29] J. Fu, K. Liu, K. Jiang, et al., Adv. Sci. 6 (2019) 1900796.
[30] R. Zhang, Y. Li, M. Zhou, et al., ACS Appl. Mater. Interfaces 11 (2019) 26711–26721.
[31] Z. Durmus, A.W. Maijenburg, Int. J. Hydrog. Energy 47 (2022) 36784–36813.
[32] Y. Chen, M. Cheng, C. Lai, et al., Small 19 (2023) 2205902.
[33] W. Bing, Z. Chen, H. Sun, et al., Nano Res. 8 (2015) 1648–1658.